Contents lists available at ScienceDirect

Electrochimica Acta

Impact of Interfacial Water Transport in PEMFCs on Cell Performance

Toshikazu Kotaka [a,*], Yuichiro Tabuchi [a], Ugur Pasaogullari [b], Chao-Yang Wang [c]

[a] EV System Laboratory, Research Division 2, Nissan Motor Co., Ltd. 1, Natsushima-cho, Yokosuka-shi, Kanagawa 237-8523, JAPAN
[b] Department of Mechanical Engineering/Center for Clean Energy Engineering, University of Connecticut 44 Weaver Rd., Unit 5233, Storrs, CT, USA
[c] Electrochemical Engine Center (ECEC), The Pennsylvania State University 301C Reber Building, University park, PA, USA

ARTICLE INFO

ABSTRACT

Coupled cell performance evaluation, liquid water visualization by neutron radiography (NRG) and numerical modeling based on multiphase mixture (M2) model were performed with three types of GDMs: Micro Porous Layer (MPL) free; Carbon Paper (CP) with MPL; and CP free to investigate interfacial liquid water transport phenomena in PEMFCs and its effect on cell performance.

The visualized results of MPL free GDM with different wettability of bi-polar plates (BPPs) showed hydrophilic BPP improved liquid water transport at the interface between CP and channel. Numerical modeling results indicated that this difference with BPP wettability was caused by the liquid water coverage difference on CP surface. Thus, controlling liquid water coverage is the one of the key strategies for improving cell performance. Additionally, liquid water distributions across the cell for three types of GDMs were compared and significant difference in liquid water content at the interface between Catalyst Layer (CL) and GDM was observed. Numerical modeling suggests this difference is influenced by the gap at the interface and that the MPL could minimize this effect. The CP free cell (i.e. only MPL) showed the best performance and the lowest liquid water content. There were multiple impacts of interfacial liquid water transport both at CL-GDM and GDM-channel interfaces. High hydrophobicity and fine structure of MPLs contributed to enhanced liquid water transport at GDM-channel interface and as a result reduced the liquid water coverage. At the same time, MPL improves contact at the CL-GDM interface in the same manner as seen in CP with MPL case. Thus, the CP free concept showed the best performance. It is suggested that the design of the interface between each component of the PEMFC has a great impact on cell performance and plays a significant role in achievement of high current density operation and cost reduction in FCEVs.

1. Introduction

Polymer Electrolyte Membrane Fuel Cells (PEMFCs) are regarded as a potential alternative clean energy source for automotive applications. Key challenges to the acceptance of PEMFCs for automobiles are cost reduction and improved power density for compactness. In PEMFCs, the energy of fuel is directly converted into electricity through electrochemical reactions with platinum (Pt) as a catalyst. Since Pt is a noble metal, a reduction of total Pt usage is essential to achieve cost reduction of Fuel Cell Electric Vehicles (FCEVs) [1,2]. High current density operation is the one of the most promising solutions, since it contributes to a reduction in size as well as in Pt usage [3]. However, under high current density operation, oxygen transport in porous media and/or channels in PEMFCs becomes one of the most dominant phenomena

and strongly decreases performance [4]. At the same time, water content increases due to higher water production rate in the cathode catalyst layer (CL) as well as electro-osmotic drag through the polymer electrolyte membrane (PEM) from the anode side. Therefore, liquid water accumulates inside fuel cell components such as gas diffusion layers (GDLs) and channels. Furthermore, as PEMFCs are required to operate under various environmental conditions in automotive applications, this leads to more liquid water accumulation, especially at lower temperature or higher humidity [5,6]. This excessive liquid water significantly obstructs oxygen transport from channel to CL [7]. In order to achieve high current density operation, it is thus essential to reduce oxygen transport resistance based on full phenomenological understanding of liquid water transport inside PEMFCs.

Visualization of liquid water behavior in PEMFCs is a powerful method used to obtain understanding of liquid water transport. To date, significant research has been undertaken using optical visualization [8,9], x-ray radiography (XRG) and computed tomography (XCT) [10–12], and neutron radiography techniques [13,14]. Zhang

* Corresponding author. Tel.: +81 46 867 5348.
  E-mail address: t-kotaka@mail.nissan.co.jp (T. Kotaka).

Nomenclature

I	transmitted intensity
I_0	incident intensity
t	water thickness m
A	cross sectional area or defined in Equation (24)
C_{sat}	concentration of the saturated water vapor mol m^{-3}
C_p	specific heat capacity J kg^{-1} K^{-1}
C	concentration mol m^{-3}
D	diffusion coefficient m^2 s^{-1}
F	Faraday constant =96485 C mol^{-1}
J	Leverett function
j	volumetric transfer current density A m^{-3}
i_0	exchange current density A m^{-3}
j_l	capillary diffusion mass flux kg s^{-1}
K	absolute permeability m^2
k_{rk}	relative permeability of phase k
k	thermal conductivity W m^{-1} K^{-1}
m	molecular weight of liquid kg mol^{-1}
mf_k	mass fraction of phase k
p	pressure Pa
R	universal gas constant =8.314 J mol^{-1} K^{-1}
$R_{O2,CCL-micro}$	micro transport resistance near Pt surface s m^{-1}
S	source term
s	liquid saturation
T	temperature K
$\bar{u}$	velocity m s^{-1}
vrf	volumetric roughness factor m^2 m^{-3}
d_{liq}	radius of liquid water droplet m
S_{liq}	cross-sectional area of liquid water droplet m^2

Greek letters

$n\sigma$	neutron attenuation coefficient m^{-1}
α	transfer coefficient in Butler-Volmer equation
γ_c	advective correction factor
ε	porosity
η	overpotential V
θ_c	contact angle of component c
κ	proton conductivity S m^{-1}
λ	relative mobility
ν	kinematic viscosity m^2 s^{-1}
ρ	mass density kg m^{-3}
σ	electrical conductivity S m^{-1} or surface tension N m^{-1}
τ	shear stress N m^{-2}

Superscripts

eff	effective
i	species i

Subscripts

c	cathode
ch	gas flow channel
k	phase k
g	gas phase
l	liquid phase
O_2	oxygen
ref	reference
w	water
h	heat

et al. conducted optical visualization to understand liquid water removal from PEMFCs by applying a transparent plate as bottom of channels and revealed that liquid water behavior inside channel was strongly affected by the gas velocity and wettability of bi-polar plates (BPPs) [8]. Fukuyama et al. also conducted optical visualization of liquid water across the cross section of ribs and channels and showed a difference in the shape of the liquid water droplets in channels with different wettability of BPPs [9]. Hydrophilic BPPs attracted liquid water and hence reduced the liquid water coverage on the surface of the GDLs.

Optical visualization can provide qualitative understanding of liquid water behavior inside the channel due to its fine temporal resolution. However, it is difficult to obtain information on liquid water distribution inside the GDM. As such, techniques such as XRG and NRG have the ability to visualize liquid water inside the GDM, since x-rays and neutrons are able to penetrate GDM and they are attenuated and/or scattered by liquid water. Deevanhxay et al. [10] and Hinebaugh et al. [11] succeeded in visualization of liquid water distribution in PEMFCs components such as polymer electrolyte membrane (PEM), CL, GDM and channel with several μm spatial resolution and several seconds temporal resolution by optimizing x-ray beam energy. Deevanhxay et al. applied soft x-ray to obtain radiographs of MEA and revealed that lack of micro porous layer (MPL) between CL-CP caused liquid water accumulation at this interface, suppressed oxygen transport and decreased cell performance qualitatively [10]. Hinebaugh et al. showed liquid water accumulation at the delaminated regions between CL-GDM and suggested that the accumulated liquid water hindered the oxygen transport and decreased cell performance [11]. These results pointed out the impact of liquid water behavior at CL-GDM interface. Due to its high temporal and spatial resolutions, XRG is able to visualize dynamic liquid water behavior within very fine structures such as CL and MPL. However quantification of liquid water is challenging, since the difference in attenuation water and carbon, the primary material of GDM is minimal. Additionally, it is necessary to use a specially designed cell for XRG experiments due to high attenuation of x-rays by metallic PEMFC components. This change in the design may cause a change in the mass transport phenomena in PEMFC. On the other hand, the neutron beam has high sensitivity only to hydrogenous materials (e.g. water) while metals and carbon are relatively transparent to neutrons [15], providing an advantage for NRG in in-situ quantification of liquid water inside PEMFC despite lower spatial and temporal resolution. A number of researchers have successfully used NRG to determine the effect of flow field on liquid water distribution in PEMFCs [13,14]. Fu et al. visualized liquid water in a cell assembly similar to PEMFC, in which water vapor was intentionally condensed in GDMs by controlling cell temperature and dew point of feed gas, and succeeded in quantifying liquid water distribution in thru-plane direction with spatial resolution around 25 μm [13]. Turhan et al. showed the difference between hydrophilic and hydrophobic BPPs by applying NRG to operating PEMFCs [14]. Results showed lower surface coverage with hydrophilic BPPs causing an overall lower liquid water content in GDM, which also indicated the importance of liquid water behavior at the interface between GDM and channel. Similar visualization studies provided deeper understanding of liquid water behavior; however visualization itself is not sufficient to obtain a quantitative relationship between liquid water transport and cell performance. In this respect, numerical modeling at single cell level can be helpful.

We have previously [16] developed a numerical model to account for the interfacial effect of liquid water, which is shown to have large impact on cell performance [10,11,14], based on the multiphase mixture (M2) model [17]. In this study, coupled cell performance measurements, liquid water visualization by NRG, and numerical modeling were performed to quantify the influence of liquid water behavior at the interfaces of PEMFC components on the cell performance, aiming to provide insight into mass transport phenomena at high current density operation and further cost reduction.
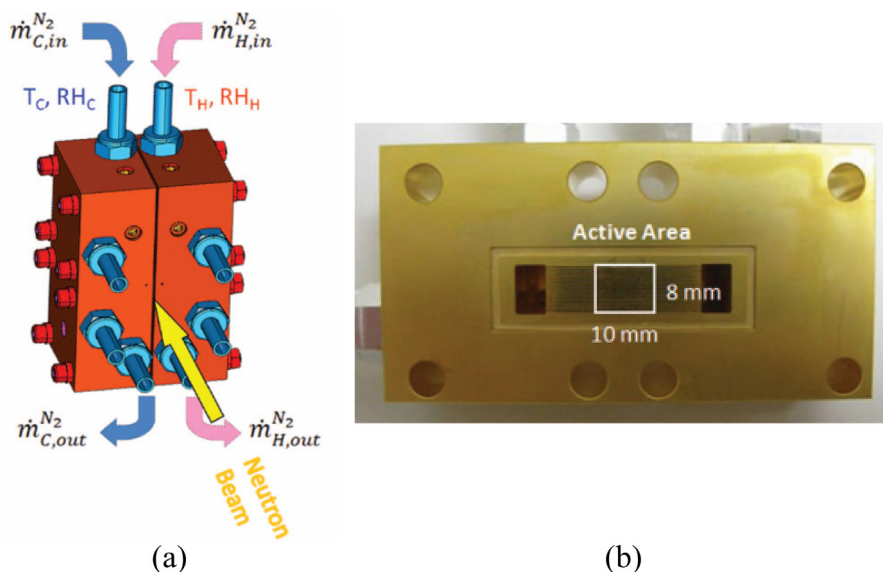
Fig. 1. (a) A schematic drawing of cell assembly. (b) A gold-plated aluminum alloy 6061 BPP. The indicated active area box represents the observation area with NRG.

2. Experimental methods

In this study, NRG was utilized for visualization of liquid water in operating PEMFCs. As discussed previously, NRG has an advantage in quantifying liquid water inside the PEMFC as its high sensitivity to liquid water allows determination of both the averaged liquid water distribution along the channel flow in the thru-plane direction, and the effect of cell components (e.g. BPP wettability) and operating conditions. Continuing improvement in neutron detection in recent years resulted in a high-resolution micro-channel plate (MCP) detector, which was utilized in this study. The MCP detector with an intrinsic resolution of around 10 μm has made water measurement in the thru-plane direction possible [13].

A specially designed cell was prepared to study water distribution in the thru-plane direction and the effect of interfaces. Fig. 1 shows a schematic of the cell assembly. The hardware consisted of a pair of gold-coated aluminum alloy 6061 end plates with machined central flow-field, silicone gaskets for sealing, and coolant fluid loops surrounding the flow-field for precise control of cell temperature, which strongly affects liquid water transport process. The coolant loops were designed so as not to obstruct the field-of-view of a neutron beam. K-type thermocouples were embedded 1.0 mm beneath the flow field to monitor cell temperature near the region of interest (ROI). The effect of interfaces on liquid water transport is the focus of this study, and the surface property of flow fields is an important parameter that controls the behavior of liquid water at the GDM-channel interface. Since the gold coated aluminum alloy used for BPPs is hydrophilic, PTFE coating was applied on one set to render them hydrophobic.

Cell specifications and test conditions are summarized in Table 1. An in-house catalyst coated membrane (CCM) consisting of Pt/C catalyst layer and Nafion® membrane, NRE211 (25 μm), was placed between three types of GDMs: MPL free (Carbon paper (CP) only); CP with MPL; and CP free (MPL only) to make the membrane electrode assembly (MEA). Toray carbon paper, TGP-H-060 (190 μm) without PTFE treatment and in-house MPL made of carbon particles and PTFE with a thickness of 100 μm were utilized as CP and MPL respectively. The MEA was compressed with silicone gaskets and PTFE sheets by the BPPs. PTFE sheets worked as a spacer for controlling the compression of MEA. In order to minimize the effect of ribs and channels geometry on liquid water distribution, straight flow fields with fine ribs and channels of 0.2 mm width

Table 1
Cell specifications and test conditions.

Membrane	Nafion®, NRE211 (25 μm)
Catalyst layer	Pt/C, 0.35 mg cm^{-2} Pt loading on both sides
GDMs	Toray, TGP-H-060 (190 μm, untreated, without MPL)
	Toray, TGP-H-060 (190 μm, untreated) with in-house MPL (100 μm)
	In-house MPL (100 μm)
Flow field plate	Straight channel, ribs/channels = 0.2mm/0.2mm
Contact angle of BPPs	Hydrophilic: 50deg., Hydrophobic:120 deg.
Cell Temperature	333 K
Dew-point (Relative humidity)	333 K (100 % RH) at both sides
Inlet pressure	200 kPa.abs. at both sides
Gas species	H$_2$ at anode, Air at cathode
Gas flow rate	2 L m^{-1} at both sides

were utilized. The dimensions of active area were height of 10 mm and width of 8 mm. Such a small active area enabled neglect of the distribution in flow direction. A fuel cell test stand consisting of an electronic load, bubbler based humidifiers, and mass flow controllers was employed to measure polarization curves and conduct NRG in-situ visualization under steady state condition. Cell temperature was set at 333 K using coolant loops and dew points of both anode and cathode sides were set at 333 K, corresponding to 100% relative humidity (RH) to enhance liquid water formation. In order to maintain uniform reaction and gas concentration distribution along the flow direction, high gas flow rate of 2 L•m^{-1} was fed into both sides. A milliohm meter was used to measure high frequency resistance (HFR) at 1 kHz with 4 mA superimposed current to obtain internal resistance (IR) corrected cell voltages.

NRG measurement was performed at the Neutron Imaging Facility of the National Institute of Standards and Technology (NIST) Center for Neutron Research (NCNR) using a MCP detector with pixel pitch of 5 μm. To reduce random uncertainties from neutron counting statistics, 10 to 12 images taken with 5 minutes exposure time were averaged at each condition. The background image was subtracted from the averaged images to correct for noise effect. Finally, wet images were divided by a dry reference image. Here, wet images refer to the averaged images taken drawing a certain current density, and dry images refer to the averaged images taken under non-humidified gas condition. Thus

Table 2
Specifications of neutron radiography imaging.

Aperture (x: height, y: width)	x: 1 mm, y: 10 mm
Active area-Detector distance	26 mm (including MCP thickness)
Detector-Aperture Distance	6 m
Detector Pixel Pitch	5 μm
Data acquisition time	300 s/ image
Water attenuation coefficient	0.385 mm^{-1}

the water thickness can be evaluated based on the Beer-Lambert law (1) with predetermined neutron attenuation coefficient [13].

$$\ln\left(\frac{I_0}{I}\right) = n\sigma t \tag{1}$$

where I is the transmitted intensity, I_o is the incident intensity, and t is the water thickness being measured. The product $n\sigma$ is sometimes called as the neutron attenuation coefficient of a material with unit of inverse length. Measured thickness of water was then laterally averaged in flow direction to give an averaged thickness profile in the thru-plane direction. The specifications of the NRG experiments are summarized in Table 2.

3. Numerical model

This study employed new sub-models incorporated into three-dimensional (3-D), two-phase, non-isothermal M2 model [17,18]. The sub-models were implemented to account for micro oxygen transport resistance near Pt surface, r [19], the effect of interaction between liquid water in channels and GDM, and the effect of gap between CL-GDM on liquid water transport [16]. The model includes the following assumptions: (i) ideal gas mixtures, (ii) isotropic and homogeneous porous media, (iii) incompressible and laminar flow due to small pressure gradients and flow velocity, and (iv) treatment of gas channels as porous media due to similarity of random porous media and regular ordered pores with size less than 1 mm.

3.1. Governing equations

The model used in this study was based on M2 model as follow [17,18].
The mass conservation equation is given by

$$\nabla \cdot \left(\rho \vec{u}\right) = 0 \tag{2}$$

where u is the superficial mixture velocity and ρ is the mixture density given as

$$\rho = s \cdot \rho_l + (1 - s) \cdot \rho_g \tag{3}$$

Here, ρ is density and the subscript of l and g represents the liquid and gas phase, respectively, and s and $(1-s)$ denote the volume fraction of the pores of porous media occupied by liquid phase and vapor phase, respectively, and described as

$$s = \frac{\rho m f_w - C_{sat}m}{\rho_l - C_{sat}m} \tag{4}$$

where mf_w is mass fraction of the two-phase mixture (i.e water), C_{sat} is water saturation concentration, and m is molar weight of water.
The momentum conservation equation is given by

$$\frac{1}{\varepsilon^2}\nabla \cdot \left(\rho\vec{u}\vec{u}\right) = -\nabla p + \nabla \cdot \tau + S_u \tag{5}$$

where ε is porosity, p is pressure, τ is shear stress, and S_u is source term for momentum. The species conservation equation is given by

$$\nabla \cdot \left(\gamma_c \vec{u}C^i\right) = \nabla \cdot \left(\rho D_g^{i,eff}\nabla C_g^i\right) + \nabla \cdot \left[\left(m_g^i - m_l^i\right)\vec{j_l}\right] + S_i \tag{6}$$

where $D_g^{i,\,eff}$ is the effective diffusivity of species i of vapor phase, accounting for tortuosity and porosity, C_i is concentration of species i, m_k is mass fraction of phase k, and S_i represents source term for species conservation. The term on the left hand side of equation (6) represents the advective term with the mixture phase velocity. The gas and liquid phases have different velocities; therefore, the convective term of the mixture is corrected by an advection correction factor of γ_c

$$\gamma_c = \frac{\rho}{C^w}\left(\frac{\lambda_l}{M_w} + \frac{\lambda_g C_g^w}{\rho_g}\right) \quad \text{for water} \tag{7}$$

$$\gamma_c = \frac{\rho\lambda_g}{\rho_g(1-s)} \quad \text{for non} - \text{condensing species} \tag{8}$$

where relative mobilities of each phase, λ_k, are

$$\lambda_k = \frac{k_{rk}/\nu_k}{\sum k_{rk}/\nu_k}, \quad \sum \lambda_k = 1 \tag{9}$$

and relative permeability of individual phases, k_r, is defined as the ratio of the intrinsic permeability of phase k at a given saturation to the total intrinsic permeability as follows.

$$k_{rl} = s^4, \quad k_{rg} = (1-s)^4 \tag{10}$$

The second term on the right hand side of equation (6) describes the capillary transport and the capillary flux of the liquid phase, j_l, is given by

$$\vec{j_l} = \frac{K}{\nu}\lambda_l\lambda_g\nabla P_c \tag{11}$$

where K is permeability and the capillary pressure, P_c, described as follows with the Leverett function, $J(s)$ [20,21].

$$P_c = \sigma\cos\theta\left(\frac{\varepsilon}{K}\right)^{1/2}J(s) \tag{12}$$

$$J(s) = 1.417s - 2.120s^2 + 1.263s^3 \quad \text{for hydrophobic} \tag{13}$$

$$J(s) = 1.417(1-s) - 2.120(1-s)^2 + 1.263(1-s)^3 \quad \text{for hydrophilic} \tag{14}$$

The energy conservation equation is given by

$$\nabla \cdot \left(\gamma_h\rho C_p\vec{u}T\right) = \nabla \cdot \left(k_{eff}\nabla \cdot T\right) + S_T \tag{15}$$

where C_p is specific heat capacity of mixture, k_{eff} is effective thermal conductivity, T is temperature, and S_T is the source term for energy equation. The term on the left hand side of equation (15) represents the convective transport of energy and is similarly corrected via an advection correction factor, γ_h, given as following.

$$\gamma_h = \frac{\rho\left(\lambda_l c_{p,l} + \lambda_g c_{p,g}\right)}{s\rho_l c_{p,l} + (1-s)\rho_g c_{p,g}} \tag{16}$$

The source term in equation (15) represents heat generation, which includes entropic heat, irreversible heat of the electrochemical reaction, and the joule heating related to proton and electron transport. In addition, the latent heat transfer due to water evaporation and condensation are also included. The charge conservation equations of proton and electron are given by

$$0 = \nabla \cdot \left(\sigma_{eff}\nabla \cdot \phi_s\right) + S_{\phi s} \tag{17}$$

$$0 = \nabla \cdot \left(\kappa_{eff}\nabla \cdot \phi_e\right) + S_{\phi e} \tag{18}$$

respectively. Here, σ_{eff} is electrical conductivity, κ_{eff} is proton conductivity and S represents source term due to charge transfer. The details of the source terms in each equation can be found in reference [3].
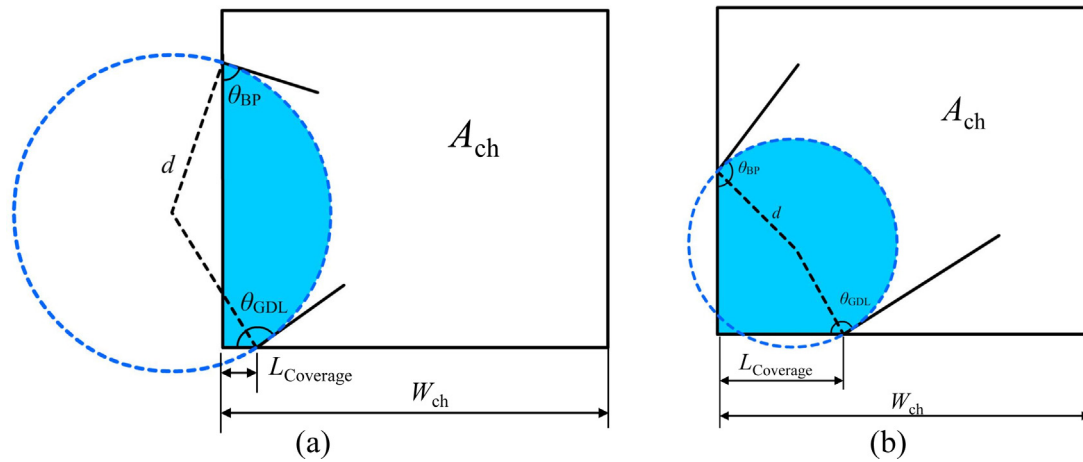
Fig. 2. Schematics of water behavior in a channel with (a) hydrophilic channel walls and (b) hydrophobic channel walls.

3.2. Droplet Model

In the original model, the effect of interfacial liquid water behavior at GDM-channel interface, in other words the influence of BPPs surface property, was not considered. In order to take it into consideration, a new boundary model, called the Droplet model, was developed and utilized. As delineated by visualization studies of water emergence at the GDM-channel interface, droplets formed on the GDM surface, and grew along the channel sidewall [9]. Physically, different wettability of the sidewall should result in different water behavior in channels and hence resulting difference of water coverage at the interface. For a hydrophilic sidewall, droplets will be attracted to the sidewall due to capillary force, leading to lower water coverage at the interface. On the other hand, for a hydrophobic sidewall, the emerged water will keep relatively spherical shape thus having larger water coverage. This coverage change with different contact angle of BPPs were implemented in the Droplet model with the following assumptions: i) only single droplet exists on a channel wall, ii) a droplet has a spherical shape defined as contact angles of sidewall and GDL surface, as shown in Fig. 2.

Based on the geometrical analysis, in the case of hydrophobic GDM, it is possible to obtain the relationship between two dimensional (2D) water coverage length on GDL, $L_{coverage}$, and liquid water saturation in the channel, s_{ch}, as follows.

For hydrophilic BPP

in this model, different boundary conditions were utilized at the interface under the covered area and not covered area as follows.

$$\vec{j}^{i} = 0 \quad \text{for } covered \text{ area} \tag{21}$$

$$\vec{j}^{i} = \vec{j}^{i}_{total} \quad \text{for } non-covered \text{ area} \tag{22}$$

Under the covered area, gaseous species flux is canceled and in the other area, species flux simply continues at the interface.

3.3. Bi-layer CP model

According to Fishman et al [22], Toray TGP CPs have non-uniform porosity distribution in thru-plane direction with larger porosity near the surface. The difference in porosity between the core and surface is approximately 10-20%. This porosity distribution in thickness direction causes spatial variation of permeability, and leads to a non-uniform liquid water distribution, which peaks toward CL. At the same time, surfaces of CP and CL are not smooth. The non-smooth surfaces at the interfaces result in a gap [23], and form the surface region, which has relatively large porosity and permeability. In order to represent this interfacial effect on liquid water transport, bi-layer CP model was implemented in this study. In this model, CP is considered to consist of two layers with different porosity and permeability. The properties of those two layers are described later.

$$L_{coverage} = \left(\sin\theta_{GDL} - \cos\theta_{BPP}\right)$$

$$. \sqrt{\frac{A_{ch}s_{ch}}{\pi\frac{\theta_{BPP} + \theta_{GDL} - 90°}{360°} - \frac{1}{2}\sin\theta_{BPP}\cos\theta_{BPP} + \frac{1}{2}\frac{\cos^2\theta_{BPP}\cos\theta_{GDL}}{\sin\theta_{GDL}} - \frac{1}{2}\left(\sin\theta_{GDL} - \cos\theta_{BPP}\right)^2\frac{\cos\theta_{GDL}}{\sin\theta_{GDL}}}} \tag{19}$$

For hydrophobic BPP

$$L_{coverage} = \left(\sin\theta_{GDL} - \cos\theta_{BPP}\right)$$

$$. \sqrt{\frac{A_{ch}s_{ch}}{\pi\frac{\theta_{BPP} + \theta_{GDL} - 90°}{360°} - \frac{1}{2}\sin\theta_{BPP}\cos\theta_{BPP} - \frac{1}{2}\sin\theta_{GDL}\cos\theta_{GDL} + \cos\theta_{BPP}\cos\theta_{GDL}}} \tag{20}$$

where θ_{GDL} and θ_{BPP} are contact angle of GDL surface and channel wall, respectively, and A_{ch} represents cross-sectional area of a channel. The detail of development of equations (19, 20) will be provided in appendix. This coverage length already has the effect of wettability of BPPs on water behavior in channel. Additionally,

3.4. Catalyst Layer Model

Fig. 3, a schematic of transport phenomena in the catalyst layer, shows the two types of the oxygen transport resistance [24].
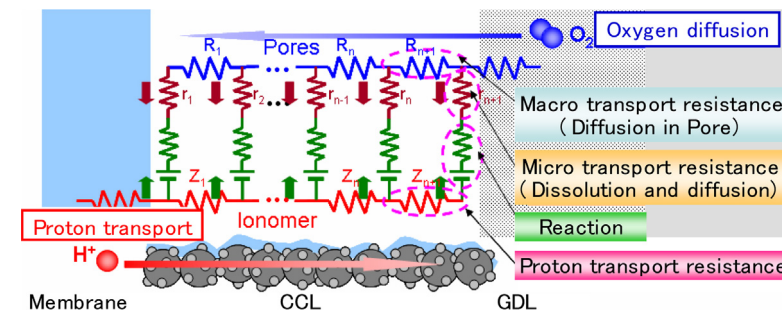
Fig. 3. Schematic of electric circuit empirical model of transport phenomena in the catalyst layer.

One type is oxygen transport resistance in the thickness direction through secondary pores, which are several tens of nm. The other type is oxygen transport resistance toward the Pt surface. Here, the Knudsen diffusion resistance in the secondary pore is called the macro transport resistance, expressed by $R_{O2, CCL-macro}$ as represented in the reference [19]. Furthermore, the local transport resistance near Pt through ionomer and/or water is defined as the micro transport resistance, referred to as $R_{O2, CCL-micro}$. In this work, the effect of $R_{O2, CCL-macro}$ was expressed in the diffusion coefficient as pressure independent effective diffusivity while the other effect was implemented to modify the source term of oxygen in species conservation as follows.

$$S_{O_2} = \frac{j}{4F} = \frac{A \cdot C_{O_2,bulk}}{4F \cdot C_{O_2,ref}} \left(\frac{4C_{O_2,ref} \cdot F \cdot vrf}{4C_{O_2,ref} \cdot F \cdot vrf + A \cdot R_{O_2,CCL-micro}} \right) \quad (23)$$

where F is Faraday constant, vrf is volumetric roughness factor, and A is defined as follows.

$$A = -ai_0 \exp\left(-\frac{\alpha_c F}{RT} \eta \right) \quad (24)$$

where ai_0 is the production of effective Pt surface area and exchange current density, α is the transfer coefficient, R is the universal gas constant, and η represents the over potential. The transfer coefficient is obtained from reference [4] and ai_0 was determined by fitting the polarization curve of the MPL free case with hydrophilic BPP under which mass transport loss was negligible. The detail can be found in Ref. [19].

3.5. Transport, Kinetic, and Material Properties for Numerical Study

The effective oxygen diffusion coefficient in the CP was experimentally determined by limiting current method [25,26] with CPs of different thicknesses. More detailed information can be found in reference [27]. For measuring of oxygen transport resistance in MPL, due to relatively small thickness, an ex-situ method, which can reduce the effect of rib/channel geometry on oxygen transport phenomena are preferred. In this study, the value measured by Yokoyama et. al [28] with a mutual diffusion method was utilized. The effective Knudsen diffusion coefficient in CLs was analytically estimated based on the pore size distribution [29]. Here, pores with diameter, more than 10 nm were regarded as the secondary pores those contribute to Knudsen diffusion. Based on the assumed simple transport model in the CL, the oxygen transport resistance toward Pt surface, $R_{O2, CCL-micro}$, was separated in Ref. [29].

Volumetric roughness factor and effective Pt surface area were experimentally evaluated by cyclic voltammetry. Porosity of materials was measured by mercury intrusion porosimetry (MIP) method for CPs and CLs, and mass-measuring method [28] was utilized for MPLs. For CPs and MPLs, the effect of compression was considered by calculating the change based on the thickness as assembled. Based on this porosity, permeability was calculated

Table 3
Material properties in numerical analyses.

CP porosity	-	0.65
CL porosity	-	0.4
CP permeability	m²	2.9×10^{-12}
CL permeability	m²	8.4×10^{-13}
CP contact angle	°	115
MPL contact angle	°	145
CL contact angle	°	91
Hydrophilic BPP contact angle	°	50
Hydrophobic BPP contact angle	°	120
CP thermal conductivity	W·m⁻¹·K⁻¹	1.0
MPL thermal conductivity	W·m⁻¹·K⁻¹	0.27
CL thermal conductivity	W·m⁻¹·K⁻¹	0.64
PEM thermal conductivity	W·m⁻¹·K⁻¹	0.95
BPP thermal conductivity	W·m⁻¹·K⁻¹	110.0
CP electrical conductivity	S·m⁻¹	936.0
MPL electrical conductivity	S·m⁻¹	230.0
CL electrical conductivity	S·m⁻¹	230.0
BPP electrical conductivity	S·m⁻¹	4800.0
Volume fraction of ionomer in CL	-	0.2

with T-S model [30] for the CP case. For MPL, in order to obtain enough robustness of calculation, one-hundredth of the permeability of CPs was utilized. In previous studies, the wide range of MPL permeability was employed [20,31,32] and that value is in the range. The sessile drop method was utilized to measure the contact angle. Thermal conductivity of each component was measured with steady-state thermal flux method [33], and electrical conductivity was obtained with two probe method with materials of different thicknesses [27]. Those are summarized in Table 3. PEM properties such as water uptake, proton conductivity, electro osmotic drag coefficient and water diffusivity were obtained from reference [19].

In this study, bi-layer CP model was utilized for considering interfacial liquid water transport effect on cell performance. In Table 4, main properties for bi-layer CP model for MPL free case were summarized. It was assumed that the surface region of CPs has a 15% higher porosity than that of the core region, consistent with the results of Fishman et al [22]. For CP with MPL case, it was assumed that the gap and/or porosity distribution effect can be dismissed, since MPL has relatively lower mechanical strength and can be easily deformed and fill the surface region of CP. In this case, the properties of the surface region were replaced with that of MPL as shown in Table 5.

Table 4
Material properties for bi-layer model of MPL free case.

CP core porosity	-	0.65
CP surface porosity	-	0.74
CP core permeability	m²	2.9×10^{-12}
CP surface permeability	m²	8.4×10^{-12}
CP core thickness	μm	130
CP surface thickness	μm	20

Table 5
Material properties for bi-layer model of CP with MPL case.

CP core porosity	-	0.65
MPL porosity	-	0.6
CP core permeability	m^2	2.9×10^{-12}
MPL permeability	m^2	2.9×10^{-14}
CP thickness	μm	150
MPL thickness	μm	100

4. Results and discussions

4.1. MPL free case

The visualized liquid water distribution of cross sectional view of MPL free MEA at a current density of 0.5 A·cm^{-2} is shown in Fig. 4. Some amount of liquid water was recognized in PEM, CP, and channel, especially at the interface between CL-CP in cathode side. At the same time, the water thickness in the MEA with hydrophobic BPPs was higher than that with hydrophilic BPP. For clarification, liquid water thickness distributions of both hydrophilic and hydrophobic cases in the cathode side -averaged in the flow direction- were compared in Fig. 5. The visualization results illuminate two points. First, the visualization results clearly confirmed that liquid water saturation in CP with hydrophobic BPP was 25 to 60% larger than that with hydrophilic BPP. These results qualitatively agree with previous studies [9,14]. That is, due to the difference of surface energy of the CP and the BPP, liquid water in a channel easily spreads along the channel wall of a hydrophilic BPP by capillary action, while in the case of hydrophobic BPP, it grows on the surface of the CP. This leads to a difference of liquid water coverage ratio on the surface of CP as the droplet model accounts for. Thus, the wall of the hydrophilic BPP contributed to decrease in liquid water inside the CP. On the other hand, when the hydrophobic BPP was used, the liquid water could not easily move toward the channel wall and coverage length of liquid water increased, resulting in relatively higher liquid water saturation in CP.

The second point clarified through the visualization results was liquid water accumulation at the interface between CL-CP. It can be clearly recognized that there was a peak of liquid water
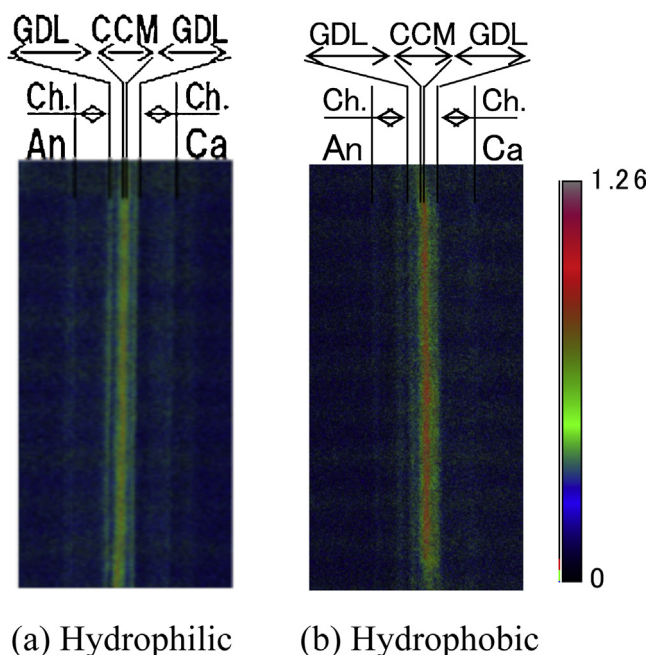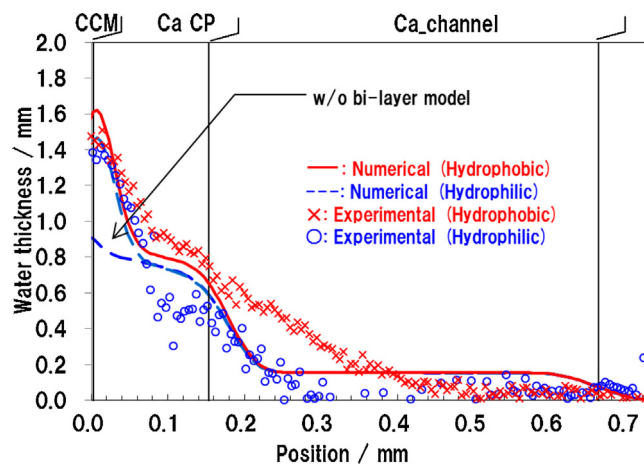

Fig. 5. Comparison of experimental and numerical results on liquid water thickness distribution of MPL free MEA with hydrophilic and hydrophobic BPPs at 0.5 A·cm^{-2}.

saturation in CP toward CL. This peak indicated liquid water accumulation at this interface. This could be due to the influence of gap and/or surface region at the interface, both of which should have higher porosity according to previously published research [19] and result in permeability distribution in the thru-plane direction. Since liquid water in porous media is transported by the capillary pressure gradient, the higher permeability region should theoretically have higher saturation value in hydrophobic media. Thus, liquid water could easily accumulate at the CL-CP interface. In order to understand the above interfacial effects more deeply, numerical validation of experimental results was conducted as shown in Fig. 5. The numerically predicted water thickness profile was discretized according to the pitch size of neutron radiograph, computed as a weighted sum of the point spread function at each point and converted to simulated neutron radiographic profiles. This convolution process was carried out based on assuming a realistic spatial resolution of 30 μm, aperture size, active area-detector distance and active area-aperture distance. The realistic spatial resolution was derived by considering both geometric blurring effect and detector intrinsic resolution, which was calculated by fitting sharp edge of raw data of intensity distribution with an error function [15]. The numerical and experimental results showed good agreement as follows. Nevertheless, the difference between numerical and experimental results should be mentioned. It was reported [34,35] that the accuracy of NRG consistently improves, down to as low as 10% from 400%. However, 10% error was obtained merely in the membrane for a relatively simple case in which there was no water production. Additionally, due to the long acquisition time of NRG, rapid motion of liquid water cannot be captured and may contribute to the error. Thus, the error of 20-40% between experimental and numerical results can be recognized as good agreement.

When we focus on the difference in liquid water distribution with different BPP contact angle, numerical results again show similar difference with experimental data. This indicates that the Droplet model is sufficiently accurate to reveal the effect of interfacial liquid water transport at GDM-channel interface. At the same time, numerical results could predict the distinct peak of liquid water in CP near CL. However, if the bi-layer CP model was turned off, the numerical models could not predict a peak in CP toward CL as shown in Fig. 5. This fact indicates that the interfacial effect at CL-CP has an impact on liquid water transportation and it can be considered with bi-layer CP model. It is indirectly suggested that the gap and/or porosity distribution in thru-plane direction increased liquid water content at the interface significantly.

These variations in liquid water saturation could result in the difference in oxygen transport resistance from channel to CL, thus
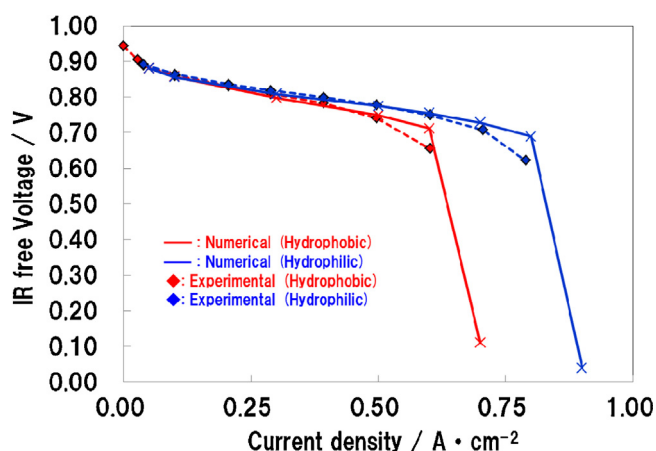

## (a) Hydrophilic	(b) Hydrophobic

Fig. 4. Visualized water thickness distribution in thickness direction with (a) hydrophilic BPPs and (b) hydrophobic BPPs.

Fig. 6. Comparison of experimental and numerical results on polarization curves of MPL free MEA with hydrophilic and hydrophobic BPPs.

Fig. 8. Comparison of experimental and numerical results on polarization curves of MPL free MEA and CP + MPL MEA with hydrophilic BPPs.

cell performance should be affected. Using those models, polarization curves of MPL free MEA with hydrophilic and hydrophobic BPPs were calculated and compared with experimental data in Fig. 6. Again, numerical results and experimental results are well correlated. From these facts, it can be said that the numerical model can explain the effect of liquid water interaction from channel to CL. Interfacial water transport effect on cell performance was established by implementing Droplet and bi-layer CP sub-models into the M2 model. These results revealed the importance of interfacial liquid water transport at GDM-channel and CL-GDM interfaces for decreasing liquid water content inside MEA to achieve higher current density operation and increase robustness of PEMFCs.

4.2. CP with MPL case

Through the study with MPL free MEA, it was confirmed that interfacial liquid water transport at the interface between CL and GDM has a significant impact on cell performance as a result of liquid water accumulation. In order to understand MPL function at this interface, liquid water visualization and cell performance evaluation were conducted for MEA with GDM consisting of CP and MPL. Fig. 7 shows visualized liquid water distribution of CP with MPL case with hydrophilic BPPs at 1.5 A·cm^{-2} in thru-plane direction. Numerical result is also shown. In this case, the surface region parameters for bi-layer CP model were displaced with those of MPL as discussed in the section on numerical modeling. It can
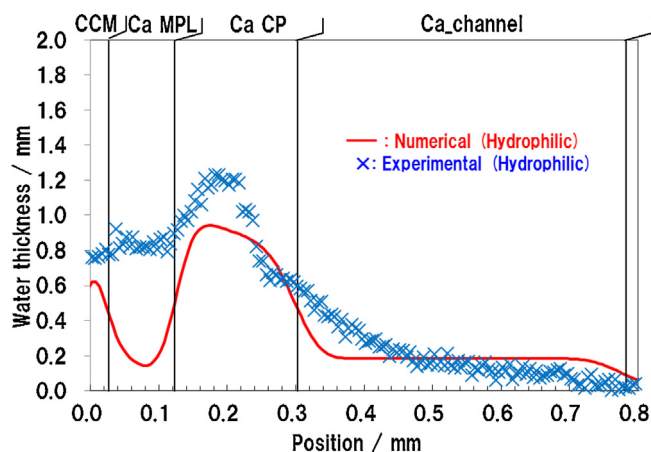

Fig. 7. Comparison of experimental and numerical results on liquid water thickness distribution of GDM consisted of CP and MPL with hydrophilic BPPs at 1.5 A·cm^{-2}.
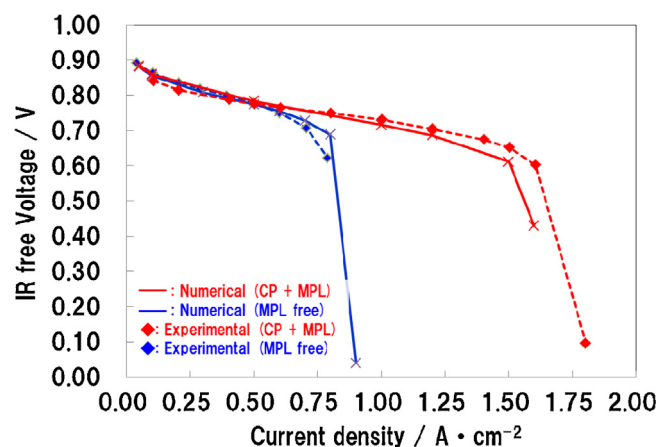
be clearly confirmed that distinct peak of liquid water content in CP near the interface of CL-GDM disappeared with application of MPL at the interface. This fact indicates that the gap and/or surface region effect on liquid water film formation was decreased by adding MPL. It also supports the assumption that MPL can fill the gap and/or high porosity region by deforming with compression pressure resulting in improved interfacial liquid water transportation. As a result, liquid water content in CL was much lower than that in MPL free case and cell performance of CP + MPL MEA was much better than that of MPL free case shown as Fig. 8. Thus, the control of MPL thickness and mechanical properties could be one of the key methods used to achieve high current density operation. However, it can be also confirmed from Fig. 7 that a large amount of liquid water still remained in the CP. For further improvement of cell performance, this study attempted the necessary reduction of that liquid water remnant by removing CP from MEAs.

5. CP free case

Tabuchi et al. [36] revealed that it is possible to achieve higher cell performance by removing carbon paper, since CP is shown to dominate the oxygen and electron transport resistance in fuel cells [37,38]. However, mass transport phenomena -especially liquid water transport- in CP free cell is not fully understood. In the previous section, it was revealed that reduction of the interfacial resistance of liquid water transport is essential to reduce liquid water content in MEA and improve cell performance. This section focuses upon deeper understanding of liquid water transport phenomenon inside the CP free cell.

Fig. 9 shows liquid water content in CP free cell at a current density of 2.0 A·cm^{-2}. The comparison of polarization curves of MPL free, CP + MPL, and CP free MEA was conducted as shown in Fig. 10. As discussed in above, MPL also prevented liquid water accumulation at the interface of CL-GDM in CP free case. Liquid water content in the CL is revealed to be at very low level. Additionally, due to strong hydrophobicity and much finer structure of MPL, the liquid water coverage on GDM surface was much smaller and liquid water removal from MEA was enhanced in CP free case. For these reasons, CP free cell showed much lower total water content even with such a high current density as high as 2.0 A·cm^{-2}. As a result, CP free cell had much better performance, as shown in Fig. 10. In summary, the higher performance of CP free cell was not only caused by reduction of oxygen and electron transport resistance but also by higher water drainage ability at both interfaces of CL-GDM and GDM-channel.
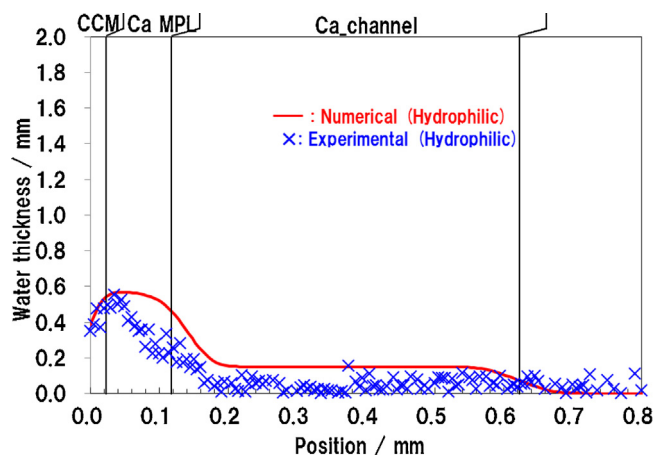
Fig. 9. Comparison of experimental and numerical results on liquid water thickness distribution of CP free case with hydrophilic BPPs at 2.0 A·cm⁻².
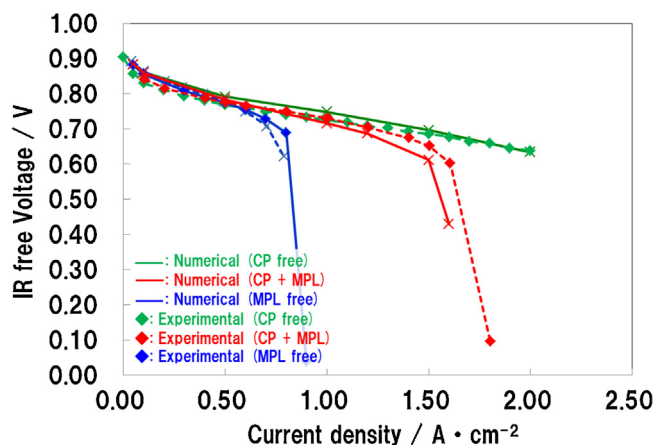

Fig. 10. Comparison of experimental and numerical results on polarization curves of MPL free, CP + MPL, and CP free MEA with hydrophilic BPPs.
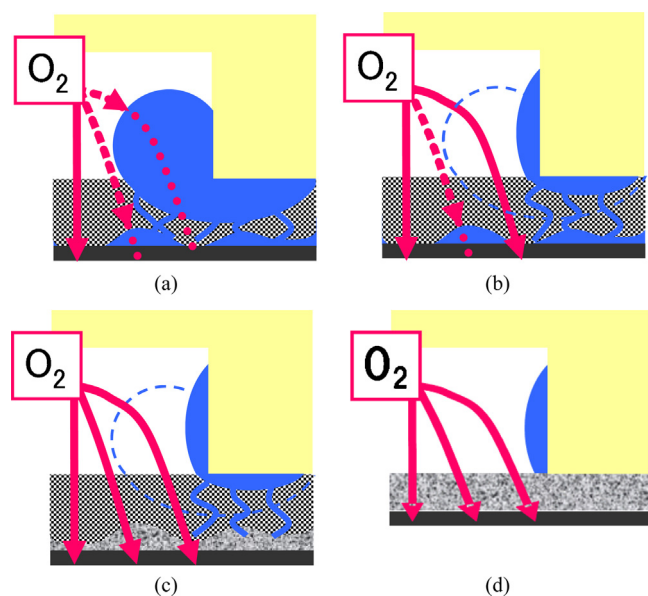

Fig. 11. Schematics of liquid water transport phenomena in (a) MPL free with hydrophobic BPP, (b) MPL free with hydrophilic BPP, (c) CP + MPL with Hydrophilic BPP, and (d) CP free with hydrophilic BPP.

6. Conclusions

Coupled cell performance evaluation, liquid water visualization by NRG method and numerical modeling based on M2 model were performed with three types of GDMs: MPL free; CP with MPL; and CP free to investigate interfacial liquid water transport phenomena in PEMFCs and its effect on cell performance. Introduction of two interfacial models into M2 model enabled qualitative insight into the impact of interfacial liquid water transport on cell performance in PEMFCs with the goal of achieving high current density operation and cost reduction.

The summary of these insights are shown as schematics of liquid water distribution in the above three types of GDMs in Fig. 11. The comparison of MPL free case with different hydrophobicity revealed the dual impact of interfacial liquid water transport on cell performance. At the interface of GDM-channel and CL-GDM interface, the key parameter is liquid water coverage change with different wettability of BPP. Hydrophilic BPP attracted liquid water, reduced surface coverage with liquid water, and enhanced liquid water removal from GDM and oxygen transport into GDM, resulting in higher cell performance than in the hydrophobic case. On the other hand, for the hydrophobic case, liquid water tended to grow along with GDM surface and obstruct mass transport at this surface. At the CL-GDM interface, due to the gap and/or surface region with relatively large porosity and permeability, liquid water easily accumulated at the interface, producing a significant increment of liquid water content in CL and hindering oxygen transport into the CL. Thus MPL free MEA showed much poorer performance. With introduction of MPL at this interface (since MPL has a relatively low mechanical strength and easily deformed by compression pressure) the gap and/or surface region was filled up and its effect was significantly decreased. Thus cell performance of MEA with CP + MPL exceeded that of MPL free case. This fact indicated that one of the functions of MPL is filling the gap between CL-CP, improving interfacial liquid water transport and cell performance. In case of CP free cell, high hydrophobicity of MPL reduced liquid water coverage ratio on GDM surface. Additionally, MPL prevented liquid water film formation at CL-GDM interface. With these double effects on liquid water transport phenomena and decrease in oxygen and electron transport resistance, CP free cell showed by far the highest performance among the three types of GDM. These results reveal the importance of interface design for achieving high current density operation while providing sufficient robustness for automobile applications and demonstrate the viability of the CP free concept as a potential solution to accomplish these important goals.

Appendix A. Appendix

Derivation of 2D water coverage length on GDM

Here the relationship between liquid water saturation in channel and liquid water coverage length on GDM will be described. Fig. A1 shows the schematic of liquid water shape in channel with hydrophilic BPPs defined by the assumption of droplet model. In

order to obtain the liquid water coverage length described as equation (A1), the radius of liquid water droplet, d_{liq}, is necessary.

$$L_{coverage} = d_{liq} \left(\sin\theta_{GDL} - \cos\theta_{BPP} \right) \tag{A1}$$

Here, the d_{liq} can be derived by considering the cross-sectional area of liquid water droplet, S_{liq}. S_{liq} on the hydrophobic GDL is

a relationship between liquid water saturation in channel, s_{ch}, and cross-sectional area of channel, A_{ch}

$$S_{liq} = A_{ch} \cdot s_{ch} \tag{A3}$$

From these equations, d_{liq} can be derived as equation (A4) and $L_{coverage}$ was developed as equation (19) by introducing it in equation (A1).

$$d_{liq} = \cdot \sqrt{\frac{A_{ch}s_{ch}}{\pi\frac{\theta_{BPP}+\theta_{GDL}-90°}{360°} - \frac{1}{2}\sin\theta_{BPP}\cos\theta_{BPP} + \frac{1}{2}\frac{\cos^2\theta_{BPP}\cos\theta_{GDL}}{\sin\theta_{GDL}} - \frac{1}{2}\left(\sin\theta_{GDL}-\cos\theta_{BPP}\right)^2\frac{\cos\theta_{GDL}}{\sin\theta_{GDL}}}} \tag{A4}$$

derived geometrically as shown in Fig. A1 (b) and described as equation (A2).

$$S_{liq} = \pi d_{liq}^2 \frac{\theta_{BPP}+\theta_{GDL}-90°}{360°} - \frac{1}{2}d_{liq}^2 \sin\theta_{BPP}\cos\theta_{BPP}$$
$$+ \frac{1}{2}d_{liq}^2 \frac{\cos^2\theta_{BPP}\cos\theta_{GDL}}{\sin\theta_{GDL}} - \frac{1}{2}d_{liq}^2\left(\sin\theta_{GDL}-\cos\theta_{BPP}\right)^2\frac{\cos\theta_{GDL}}{\sin\theta_{GDL}} \tag{A2}$$

The liquid water shape in channel with hydrophobic BPPS is schematized as Fig. A2. S_{liq} and d_{liq} are derived in same manner with hydrophilic case as following, and developing the equation (20).

$$S_{liq} = \pi d_{liq}^2 \frac{\theta_{BPP}+\theta_{GDL}-90°}{360°} - \frac{1}{2}d_{liq}^2 \sin\theta_{BPP}\cos\theta_{BPP}$$
$$- \frac{1}{2}d_{liq}^2 \sin\theta_{GDL}\cos\theta_{GDL} + d_{liq}^2\cos\theta_{BPP}\cos\theta_{GDL} \tag{A5}$$

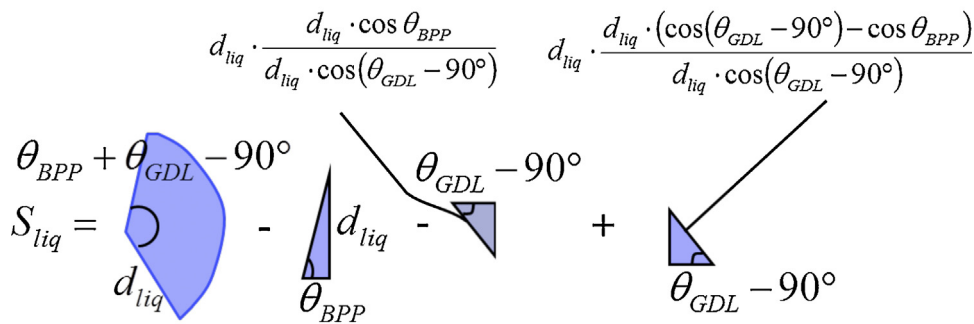$$d_{liq} = \sqrt{\frac{A_{ch}s_{ch}}{\pi\frac{\theta_{BPP}+\theta_{GDL}-90°}{360°} - \frac{1}{2}\sin\theta_{BPP}\cos\theta_{BPP} - \frac{1}{2}\sin\theta_{GDL}\cos\theta_{GDL} + \cos\theta_{BPP}\cos\theta_{GDL}}} \tag{A6}$$

where θ_{GDL} and θ_{BPP} are contact angle of GDL surface and channel wall, respectively. Here, S_{liq} can also be written in equation (A3) as
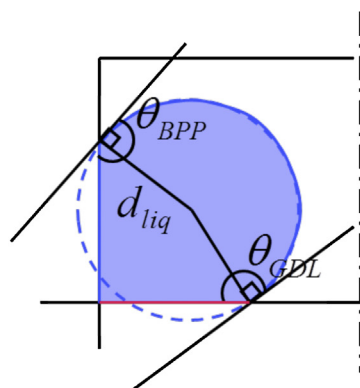
Fig. A1
Fig. A2
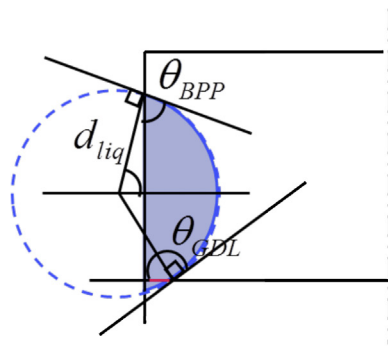
(a) 2D liquid water shape.

(b) Derivation of the liquid water cross-sectional area.

Fig. A1. The schematics of liquid water shape in channel defined by the assumption of Droplet model with hydrophilic BPPs.

(a) 2D liquid water shape.

(b) Derivation of the liquid water cross-sectional area.

Fig. A2. The schematics of liquid water shape in channel defined by the assumption of Droplet model with hydrophobic BPPs.

References

[1] B. James, J. Kalinoski, K. Baum, Mass-production cost estimation for automotive fuel cell systems, DOE Annual Merit Review (2010).

[2] M. Abe, T. Oku, Y. Numao, S. Takaichi, M. Yanagisawa, Low-cost FC Stack Concept with Increased Power Density and Simplified Configuration Utilizing an Advanced MEA, SAE (2011), 2011-01-1344.

[3] Y. Tabuchi, T. Shiomi, O. Aoki, N. Kubo, K. Shinohara, Effects of heat and water transport on the performance of polymer electrolyte membrane fuel cell under high current density operation, Electrochim. Acta 56 (2010) 352.

[4] Y. Tabuchi, T. Shiomi, Y. Fukuyama, K. Sato, N. Kubo, Higher Current Density Operation in PEMFC for Automobile applications, 222nd Meeting of ECS, Abs. 1496 (2012).

[5] D. Spernjak, S.G. Advani, A.K. Prasad, Simultaneous Neutron and Optical Imaging in PEM Fuel Cells Fuel Cells and Energy Conversion, J. Electrochem. Soc. 156 (1) (2009), B109.

[6] E. Kimball, T. Whitaker, Y.G. Kevrekidis, J.B. Benziger, Drops, slugs, and flooding in polymer electrolyte membrane fuel cells, AIChE Journal 54 (5) (2008), 1313.

[7] T. Shiomi, R. Fu, U. Pasaogullari, O. Aoki, T. Kotaka, Y. Tabuchi, N. Kubo, K. Shinohara, D.S. Hussey, D.L. Jacobson, The Influence of the Hydrophobic Treatment on the Liquid Water Transport in the Gas Diffusion Layers of the Polymer Electrolyte Fuel Cells, 218th Meeting of ECS, Abs 892 (2010).

[8] F.Y. Ahang, X.G. Wang, C.Y. Wang, Liquid Water Removal from a Polumer Electrolyte Fuel Cell, J. Electrochem. Soc 153 (2006), A225.

[9] Y. Fukuyama, T. Shiomi, O. Aoki, N. Kubo, Y. Tabushi, The Influence of the Liquid Water Behavior at the GDL-Channel Interface on Cell Performance, ECS Trans. 41 (1) (2011), 583.

[10] P. Deevanhxay, T. Sasabe, S. Tsushima, S. Hirai, Investigation of Liquid Water Accumulation in Operating PEM Fuel Cells With/Without MPL and Its Effect on Cell Performance, ECS Trans. 58 (1) (2013), 337.

[11] J. Hinebaugh, J. Lee, A. Bazylak, Visualizing Liquid Water Evolution in a PEM Fuel Cell Using Synchrotron X-ray Radiography, J. Electrochem. Soc 159 (2012), F826.

[12] P.K. Sinha, P. Halleck, C.Y. Wang, Quantification of Liquid Water Saturation in a PEM Fuel Cell Diffusion Medium Using X-ray Microtomography, Electrochem. Solid-State Lett. 9 (7) (2006), A344.

[13] R.S. Fu, U. Pasaogullari, T. Shiomi, Y. Tabuchi, D.L. Hussey, D.L. Jacobson, High-Resolution Neutron Radiography of Through-Plane Liquid Water Distribution in Polymer Electrolyte Membrane and Gas Diffusion Layer, J. Electrochem. Soc. 156 (9) (2012), F545.

[14] A. Turhan, S. Kim, M. Hatzell, M.M. Mench, Impact of channel wall hydrophobicity on through-plane water distribution and flooding behavior in a polymer electrolyte fuel cell, Electrochimica Acta 55 (2010) 2734.

[15] D.S. Hussey, D.L. Jacobson, M. Arif, K.J. Coakley, D.F. Vecchia, In Situ Fuel Cell Water Metrology at the NIST Neutron Imaging Facility, ASME Journal of Fuel Cell Science and Technology 7 (2) (2007), 021024.

[16] T. Kotaka, Y. Tabuchi, U. Pasaogullari, C.-Y. Wang, The Influence of Liquid Water Interaction between Channel, GDL and CL on Cell Performance, ECS Trans. 58 (1) (2013), 1033.

[17] Y. Wang, C.Y. Wang, Two-Phase Transients of Polymer Electrolyte Fuel Cells, J. Electrochem. Soc 154 (2007), B636.

[18] Y. Wang, S. Basu, C.Y. Wang, Modeling Two-Phase Flow in PEM Fuel Cell Channels, J. Power Sources 179 (2008) 603.

[19] Y. Fukuyama, T. Shiomi, T. Kotaka, Y. Tabuchi, The Impact of Platinum Reduction on Oxygen Transport in ProtonExchange Membrane Fuel Cells, Electrochimica Acta 117 (2014) 367.

[20] U. Pasaogullari, C.Y. Wang, Two-phase transport and the role of micro-porous layer in polymer electrolyte fuel cells, Electrochim. Acta 49 (2004) 4359.

[21] U. Pasaogullari, C.Y. Wang, Liquid Water Transport in Gas Diffusion Layer of Polymer Electrolyte Fuel Cells, J. Electrochem. Soc 151 (2004), A399.

[22] Z. Fishman, A. Bazylak, Heterogeneous Through-Plane Porosity Distributions for Treated PEMFC GDLs I. PTFE Effect, J. Electrochem. Soc. 158 (8) (2011), B841.

[23] J.H. Nam, K.-J. Lee, G.-S. Hwang, C.-J. Kim, M. Kaviany, Microporous Layer for Water Morphology Control in PEMFC, Int. J. Heat Mass Transfer 52 (2009) 2779.

[24] A. Ohma, T. Mashio, K. Sato, H. Iden, Y. Ono, K. Sakai, K. Akizuki, S. Takaichi, K. Shinohara, Analysis of proton exchange membrane fuel cell catalyst layers for reduction of platinum loading at Nissan, Electrochim. Acta 56 (2011) 10832.

[25] T. Mashio, A. Ohma, S. Yamamoto, K. Shinohara, Analysis of Reactant Gas Transport in a Catalyst Layer, ECS Trans. 11 (1) (2007) 529.

[26] D. Baker, C. Wieser, K.C. Neyerlin, M.W. Murphy, The Use of Limiting Current to Determine Transport Resistance in PEM Fuel Cells, ECS Trans. 3 (1) (2006) 989.

[27] T. Kotaka, K. Aotani, Y. Tabuchi, P. Mukherjee, The analysis of mass transport phenomena in micro porous layer for high current density operation in PEMFC for automobile application, Proceeding of ASME 2013 11th Fuel Cell Science, Engineering and Technology Conference, ESFuelCell (2013), 2013-18126.

[28] K. Yokoyama, J. Oyama, T. Tokunaga, and N. Kubo, 48th National Heat Transfer Sympojium of Japan, 2+3, B311(2011).(in Japanese).

[29] K. Sakai, K. Sato, T. Mashio, A. Ohma, K. Shinohara, Analysis of Reactant Gas Transport in Catalyst Layers; Effect of Pt-loadings, ECS Trans. 25 (1) (2009) 1193.

[30] J.T. Gostick, M.W. Fowler, M.D. Pritzker, M.A. Ioannidis, L.M. Behra, In-plane and through-plane gas permeability of carbon fiber electrode backing layers, J. Power Sources 162 (2006) 228.

[31] U. Pasaogullari, C.Y. Wang, K.S. Chen, Two-Phase Transport in Polymer Electrolyte Fuel Cells with Bilayer Cathode Gas Diffusion Media, J. Electrochem. Soc. 152 (8) (2005), A1574.

[32] Y. Ji, G. Luo, C.Y. Wang, Pore-Level Liquid Water Transport Through Composite Diffusion Media of PEMFC, J. Electrochem. Soc. 157 (12) (2010), B1753.

[33] E. Sadeghia, N. Djilali, M. Bahramib, Effective thermal conductivity and thermal contact resistance of gas diffusion layers in proton exchange membrane fuel cells. Part 1: Effect of compressive load, J. Power Sources 196 (2011) 246.

[34] A.Z. Weber, M.A. Hickner, Modeling and high-resolution-imaging studies of water-content profiles in a polymer-electrolyte-fuel-cell membrane-electrode assembly, Electrochim. Acta 53 (2008) 7668.

[35] D.L. Jacobson, D.L. Hussey, E. Baltic, M. Arif, DOE Annual Merit Review (2013), FC021.

[36] Y. Tabuchi, T. Shiomi, Y. Fukuyama, K. Sato, et al., Higher Current Density Operation in PEMFC for Automobile applications, 222th ECS Meeting Abstract, No. 1496(2012).

[37] D.R. Baker, D.A. Caulk, K.C. Neyerlin, M.W. Murphy, Measurement of Oxygen Transport Resistance in PEM Fuel Cells by Limiting Current Methods, J. Electrochem. Soc 156 (9) (2009), B991.

[38] R. Jiang, C.K. Mittelsteadt, C.S. Gittleman, Through-Plane Proton Transport Resistance of Membrane and Ohmic Resistance Distribution in Fuel Cells, J. Electrochem. Soc 156 (12) (2009), B1440.